Relaminarized and recovered turbulence under nonuniform body forces

Sandeep Pandey ,[1,2] Xu Chu ,[3,*] Bernhard Weigand,[3] Eckart Laurien,[1] and Jörg Schumacher[2]

[1]*Institute of Nuclear Technology and Energy Systems, Universität Stuttgart, Pfaffenwaldring 31, D-70569 Stuttgart, Germany*

[2]*Institute of Thermodynamics and Fluid Mechanics, Technische Universität Ilmenau, D-98684 Ilmenau, Germany*

[3]*Institute of Aerospace Thermodynamics, Universität Stuttgart, Pfaffenwaldring 31, D-70569 Stuttgart, Germany*

(Received 26 March 2020; accepted 22 September 2020; published 12 October 2020)

Turbulence in a wall-bounded flow of supercritical fluid can be significantly modulated by nonuniform body forces. This study presents direct numerical simulations performed with a nonuniform streamwise body force varying in the wall-normal direction in a fully developed channel flow. A quasilaminar state and reorganized turbulence were obtained by changing the amplitude of the nonuniform body force which distorts the parabolic mean velocity profile and thus alters the turbulence production due to mean shear. Weak production of the flattened mean velocity profile leads to a relaminarization. In the quasilaminar state, all components of the Reynolds stress tensor are fairly weak except the streamwise fluctuations distant from the wall, which indicates the collapse of the near-wall turbulence self-sustaining cycle. The remaining streamwise fluctuations away from the wall exhibit elongated streaks, which is shown by premultiplied spectra. In the recovered turbulence regime, the Reynolds shear stress has a negative range in the bulk connected with a positive range near the wall. This corresponds to the nonmonotonic shear stress resulting from an M-shaped velocity profile. In a subsequent quadrant analysis of the Reynolds shear stress, the sweep and ejection events are found to dominate near the wall only while inward Q_1 and outward Q_3 motions are significant in the bulk. Both kinds of high-speed events can be attributed to the velocity maxima of the M-shaped mean velocity profile and are found to penetrate towards the wall and the channel center. Interestingly, the flow topology shows the typical teardrop shape once turbulence recovered. Our study contributes to the understanding of flow relaminarization in mixed convection and assists in developing further flow control techniques.

DOI: 10.1103/PhysRevFluids.5.104604

I. INTRODUCTION

Supercritical fluids have attracted both engineers due to its promise of higher efficiency in energy conversion and physicists due to its highly nonlinear behavior near the critical point. There are two prominent phenomena which influence the flow physics of supercritical fluids, namely, the steep variation in thermophysical properties and in body force due to the buoyancy [1–5]. The body force itself is the result of a variable fluid density; it has the potential to influence the turbulence and to distort the mean velocity profile [4]. Several investigations exist on the combined effects of variable thermophysical properties and resulting body force on the turbulent

*xu.chu@itlr.uni-stuttgart.de

fluid flow. The characteristics of these body forces in mixed convection can then catastrophically affect the turbulence under certain circumstances. In vertical flow, the direction of fluid flow dictates the nature of heat transfer [4,6]. In buoyancy-aided flow (heated upward flow and cooled downward flow), body forces can significantly enhance the skin friction coefficient and decrease the convective heat transfer coefficient as a result of the suppression in turbulence [7]. The flow can even become laminar under very strong buoyancy forces. The velocity profile flattens out during the relaminarization [8]. The flow can recover with a new kind of turbulence with a further increase of the buoyancy force, and the mean velocity profile acquires then an M shape. This transformation into an M-shaped velocity profile is due to the external effects of buoyancy resulting from the local flow acceleration close to the wall which compensates the decrease in velocity in the core [9].

Pandey *et al.* [7] showed that the reduction in sweep and ejection events results in turbulence attenuation in downward flow under the cooling condition at supercritical pressure, while the inward and outward interaction events are responsible for a recovery in turbulence. Chu *et al.* [10] performed a Direct numerical simulation (DNS) study to examine the role of buoyancy in a strongly heated air flow through a pipe subjected to a buoyancy force. They reported that buoyancy production is suppressed compared to turbulent kinetic energy production during relaminarization. They also observed longer streaks near the wall which separated the pipe flow into two layers with an increased anisotropy in the near-wall layer. Chu and Laurien [5] conducted a DNS investigation for the horizontal flow of CO_2 with heating to reveal the effects of gravity. In this type of configuration, thermal stratification was noticed in which low-density fluid accumulates at the top of the pipe. Recently, Wetzel and Wagner [11] performed a DNS of turbulent convection in a differentially heated vertical channel. They reiterated that a buoyancy force attenuates the turbulent velocity fluctuations in the aiding flow and enhances them in the opposing flow. They also reaffirmed the indirect effect of buoyancy on the turbulent velocity fluctuations. Most of the available literature is devoted to the combined effects of body force and variable properties. However, it is important to disentangle the effects of variable material properties and body forces, which sets the motivation for the present work.

Patel *et al.* [3] have made a successful attempt to clarify the role of variable density, viscosity, and thermal conductivity in the scaling characteristics of a turbulent scalar field while omitting the effects of buoyancy force. They derived a new van Driest transformation for the mean temperature profile by incorporating the distribution of the semilocal Reynolds number. Rinaldi *et al.* [12] performed a stability analysis of DNS data of variable density and viscosity [13] and illustrated that semilocal scaling serves as an effective parametrization of the effect of variable properties on optimal streaks and their critical mode of secondary instability. Studies pertaining to the individual effect of body force have not received proper attention, but it is also very critical to expose its role in the extreme dissipative events which eventually lead to relaminarization. The DNS investigation conducted by He *et al.* [14] was an attempt to decouple these combined effects. Their DNS was performed with an artificial body force profile that resembled buoyancy-aided mixed convection. The authors observed an influence of the body force on the sweep and ejection events as well as on the anisotropy nature of turbulence. They also classified the body-force-aided flow into three regimes: partially laminarized, fully laminarized, and recovering flows based upon the strength of the imposed body force, which were similar to earlier notations of Sreenivasan [15], who categorized turbulent flow subjected to different phenomena (e.g., acceleration, suction, blowing, magnetic fields, stratification, rotation, curvature, heating, etc.) into three regimes—laminarescence, relaminarization, and retransition. There is a direct link between the strength of the body force, the turbulence modulation, the energy cascade, and the flow topology, which is still not fully understood. This knowledge can directly contribute to the flow control and the development of reduced-order models and will be addressed in the following.

Apart from the buoyancy, other body-force-influenced fluid flows are common in engineering applications [4,15,16]. Similar to the buoyancy force, the effects of the Lorenz force, which is

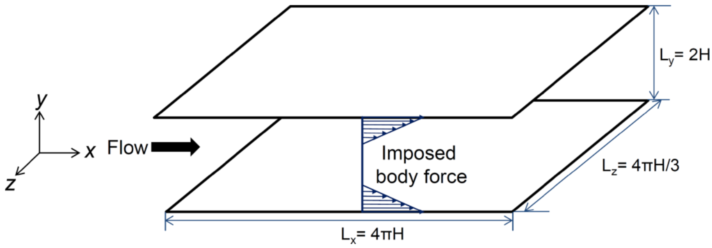

FIG. 1. Flow geometry and coordinate system. The applied body force varies only in the wall-normal direction.

a result of the magnetic field, can change the flow dynamics. Flows subjected to streamwise acceleration also show similar characteristics of turbulence attenuation [17,18]. All these different body forces act differently with a unique underlying physical principle; however, their effects on the turbulent shear flow are quite similar.

The present study aims to understand the role of a body force on the flow turbulence from the perspective of supercritical fluids. We performed a series of three-dimensional direct numerical simulations of canonical channel flow geometry with periodic boundary conditions in streamwise and spanwise directions. The incompressible flow equations are applied, thus detaching the effects of variable thermophysical properties from the body force. Special attention is given in the present work to the flow relaminarization induced by the body force. Our studies aim to examine the two-peak behavior during the recovery and understand the physics behind it better. This paper is structured in four sections. Section II describes the overall numerical approach along with the governing equations and the computational domain. Section III illustrates some important results from the DNS while focusing on the instantaneous and mean profiles, quadrant analysis, and spectral analysis, and finally, the paper concludes with a summary in Sec. IV.

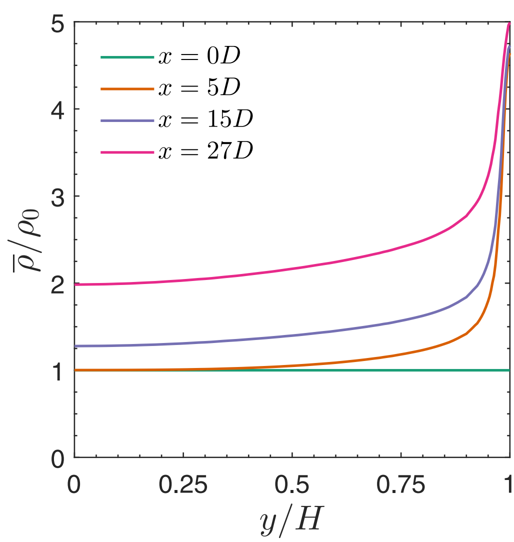

FIG. 2. Radial density profile in an upward flow under cooling conditions of supercritical CO_2 in a pipe. The pipe diameter D was 2 mm, inlet pressure was 8 MPa, and heat flux was $-61.87\ \mathrm{kW/m^2}$. Here y represents the radial direction, and H represents the radius of the pipe. Data correspond to the case UC8 of Pandey *et al.* [7].

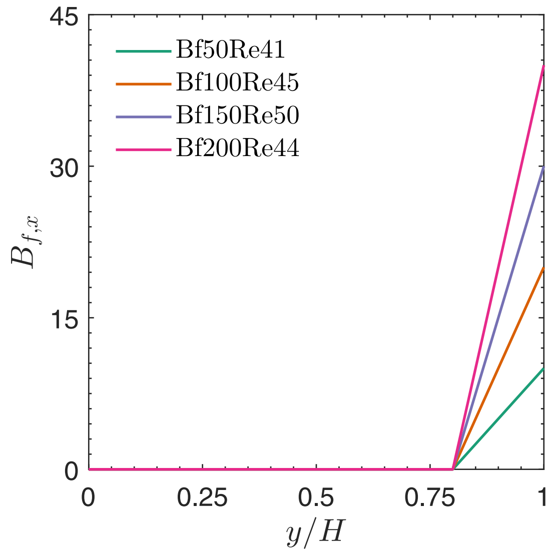

FIG. 3. Different streamwise body force distributions in the wall-normal direction which will be studied in this work.

II. NUMERICAL APPROACH

A. Computational domain and boundary conditions

In this work, an incompressible channel flow of a Newtonian fluid is considered. The channel has the dimensions $L_x \times L_y \times L_z = 4\pi H \times 2H \times 4\pi/3H$, where H is the half-channel height, as shown in Fig. 1. Periodic boundary conditions are employed in the homogeneous streamwise (x) and spanwise (z) directions, and no-slip boundary conditions are used at the walls. The flow is driven by a temporally and spatially constant streamwise pressure gradient. The body force profile can take different shapes depending on the specific physical problem. Typically, the near-wall distribution of the body force results in a peculiar phenomenon. The primary aim of this work is to investigate the body-force-influenced flow at supercritical pressure. A typical variation of the density in the wall-normal direction is shown in Fig. 2. The density $\rho(T, p)$ shows a steep variation due to the fact that temperature T and pressure p lie in the near-critical region, resulting in a localized body force due to buoyancy $\rho(T, p)\mathbf{g}$. Figure 3 illustrates the piecewise linear body force profile used in this work to approximate the complex behavior at the critical point. Only the strength of the force was varied without considering its range of coverage.

B. Governing equations and computational method

In this study, we assumed constant thermophysical properties, which enabled us to use incompressible Navier-Stokes equations. The flow-governing equations are given in Eqs. (1) and (2). In these equations, $\mathbf{u}$ denotes the velocity vector, and p is the pressure. The viscous stress is denoted by τ and defined in Eq. (3):

$$\nabla \cdot \mathbf{u} = 0, \tag{1}$$

$$\frac{\partial \mathbf{u}}{\partial t} + \nabla \cdot [\mathbf{uu} + p\mathbf{I} - \tau] = B_f(y)\mathbf{e}_x, \tag{2}$$

$$\tau = \mu[[\nabla \mathbf{u} + (\nabla \mathbf{u})^T]]. \tag{3}$$

TABLE I. Simulation parameters for all cases. Bf stands for the body force, and Re represents the Reynolds number in the name of a case. Case Bf50Re41 has a small body force corresponding to laminarescence [15]. Case Bf100Re45 is the relaminarized case. Cases Bf150Re50 and Bf200Re44 are the recovered flow cases.

Run	Case	Re_b	Re_τ	A in Eq. (4)	Δx^+	Δy^+_{min}-Δy^+_{max}	Δz^+
1	Bf50Re41	4190	256	50	8.0	0.15–2.5	5.8
2	Bf0Re41	4190	259	0	8.1	0.15–2.5	5.9
3	Bf100Re45	4565	266	100	8.3	0.15–2.7	6.1
4	Bf0Re45	4565	279	0	8.7	0.15–2.7	6.4
5	Bf150Re50	5000	310	150	9.7	0.15–3.1	7.1
6	Bf0Re50	5000	302	0	9.4	0.20–3.0	6.9
7	Bf200Re44	4490	337	200	10.5	0.20–3.3	7.7
8	Bf0Re44	4490	275	0	8.6	0.20–2.7	6.3

The body force term $B_f(y)\mathbf{e}_x$ was added to the streamwise momentum equation. The piecewise linear forcing term remains constant throughout the domain, and it is governed by

$$B_f(y) = \begin{cases} Ay, & \text{if } |y/H| > 0.8, \\ 0, & \text{if } |y/H| \leqslant 0.8. \end{cases} \tag{4}$$

DNSs are performed with the spectral/hp element solver NEKTAR++ [19,20]. A velocity correction scheme was employed in which the velocity field and the pressure are typically decoupled. Spatial discretization is based on the spectral element method in the y-z plane combined with a Fourier decomposition in the x direction. The time integration is treated using a second-order accurate mixed implicit-explicit scheme [21]. The simulation domain is discretized using a regular, structured quadrilateral mesh combined with eighth-order polynomials. Although this solver package has been used in many studies pertaining to fluid mechanics [22–25], a code verification study is performed which is relevant to the simulated cases. The corresponding results are shown in the Appendix. The y-z plane is discretized with 21×27 quadrilateral elements. The modified Legendre basis was used with eight modes (maximum polynomial order is 7). The streamwise direction contains 384 homogeneous modes. The streamwise mesh resolution normalized by the friction velocity ($\Delta x^+ = \Delta x u_\tau/\nu$, where u_τ is the friction velocity) is kept below 10.5, and the dimensionless spanwise mesh resolution was below 7.7 in every case. The mesh was refined near the wall and has a maximum dimensionless spanwise mesh width of 6.7 at the center and of 0.4 at the wall. Table I summarizes the used resolutions for the individual case.

In the present study, eight distinct cases have been simulated, four of which include a varying body force; the remaining four are reference cases simulated without body forces (runs starting with Bf0) but with the same Reynolds numbers. These cases are selected to resemble a buoyancy-aided flow. Table I shows the parameters for all simulated cases. The bulk Reynolds number is defined as $Re_b = u_b H/\nu$, where ν is the kinematic viscosity and u_b is the bulk velocity. The body force B_f follows a profile given by Eq. (4).

III. RESULTS AND DISCUSSION

Eight different direct numerical simulations are discussed in the following. The mean statistics was obtained by averaging in time and in the homogeneous spanwise and the streamwise directions. A generic variable, ϕ, was decomposed into a mean part $\overline{\phi}$ and a fluctuating component ϕ'. Instead of choosing a y^+ value, the physical coordinate y is selected due to the difference in the friction Reynolds number for cases with and without body force.

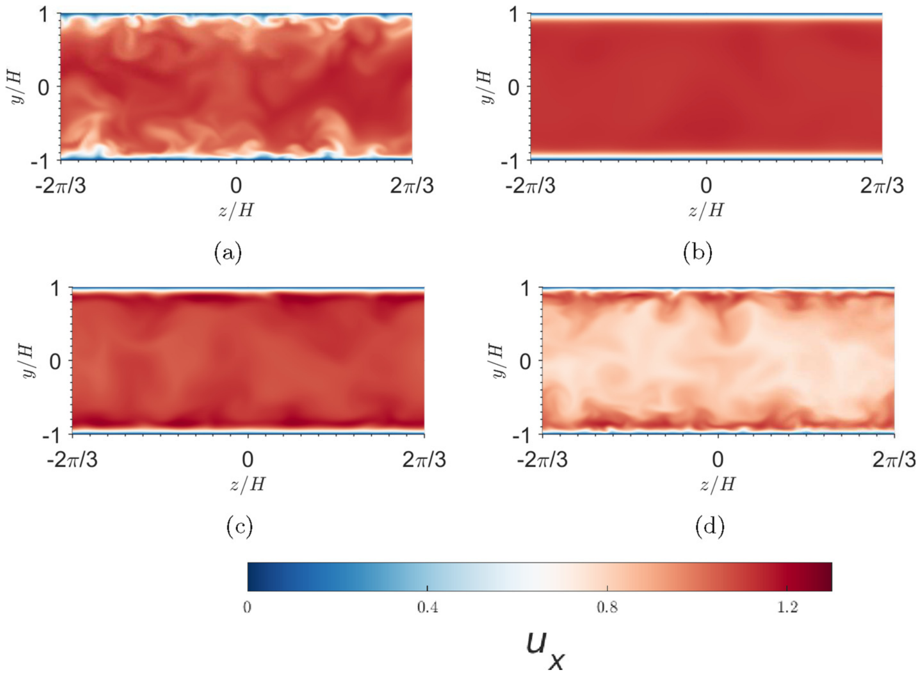

FIG. 4. Contours of the instantaneous streamwise velocity u_x, normalized by the bulk velocity u_b in the spanwise–wall-normal y-z plane. (a) Case Bf50Re41. (b) Case Bf100Re45. (c) Case Bf150Re50. (d) Case Bf200Re44. See also Table I.

A. Instantaneous and mean parameters

The qualitative change in the flow field with increasing body forces is shown in Fig. 4, where the instantaneous streamwise velocity, normalized by the bulk velocity, is depicted at one of the axial x positions. With an increase in the body force, a relaminarized state can clearly be visualized in Fig. 4(b), corresponding to case Bf100Re45. Here the fluctuating vortical structures, which are visible in Fig. 4(a), completely disappeared. With a stronger body force, a progressive flow recovery can be seen in Figs. 4(c) and 4(d). It is also noticed from Fig. 4(d) that the fluid close to the wall shows a higher velocity magnitude compared to the center in the recovered case, which is contrary to the situation shown in Fig. 4(a) under the effect of weak body force and that of a canonical turbulent channel flow without any additional body force.

The temporally and spatially (in streamwise and spanwise directions) averaged streamwise velocity profile $\overline{u}_x$ is shown in physical coordinates in Fig. 5(a) as well as in semilogarithmic wall coordinates in Fig. 5(b). As expected, the body force distorts the mean velocity profile significantly. With a relatively low value of the body force (case Bf50Re41), the velocity in the bulk decreases to compensate the increased velocity near the wall in comparison to the reference case. With a further increase of the body force magnitude (case Bf100Re45), the velocity profile flattens out. Flow relaminarization is observed in Fig. 4(b). The flattened velocity profile is in line with a smaller mean shear rate, which is essential to generate turbulence in a wall-bounded flow. A further increase of the body force in Bf150Re50 and Bf200Re44 continues to distort the mean velocity profile and leads eventually to an M-shaped mean velocity profile. The representation of the velocity in a semilogarithmic wall coordinate plot [Fig. 5(b)] shows that the profile exhibits a standard linear shape close to the wall ($y^+ \leqslant 15$). In the core region ($y^+ \geqslant 50$), the profile drops below the corresponding reference case.

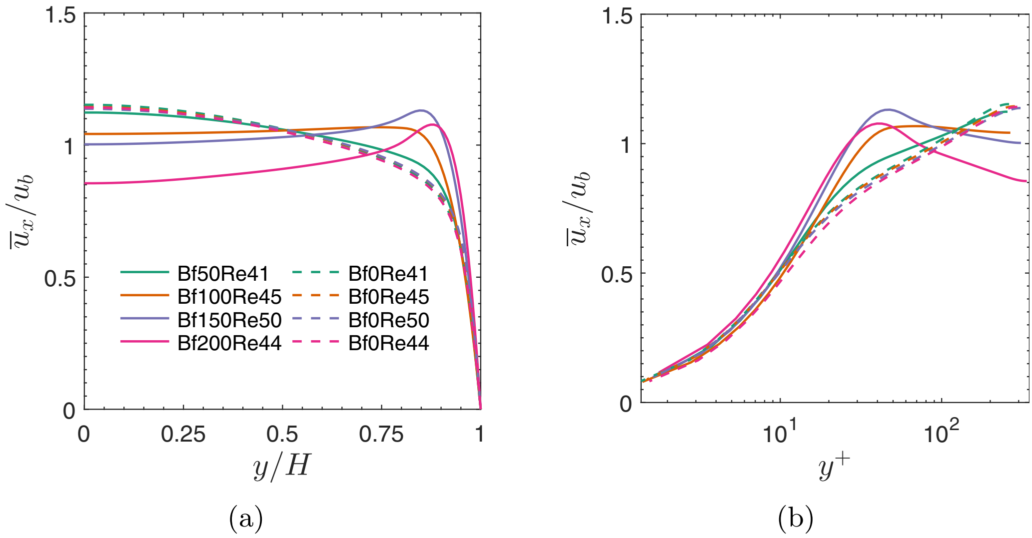

FIG. 5. Mean velocity profiles (a) in physical coordinates and (b) in wall coordinates.

The wall normal gradient of the streamwise velocity varies also with an increase in the body force, as shown in Fig. 6. The velocity gradient adjacent to the wall increases with growing body forces, which affects the wall shear stress and thereby the friction Reynolds number as listed in Table I. The M-shaped velocity profile is in line with an increase of the magnitude of the mean shear rate close to the wall. This higher magnitude assists in the turbulence recovery by an amplification of the turbulence production.

After a qualitative observation in Fig. 4, the modulation of turbulent intensity is now quantified by the rms velocity fluctuations in Fig. 7. All four fluctuations, $\sqrt{\overline{u_x'u_x'}}/u_b$, $\sqrt{\overline{u_y'u_y'}}/u_b$, $\sqrt{\overline{u_z'u_z'}}/u_b$, and $\sqrt{\overline{u_x'u_y'}}/u_b$, exhibit a similar trend; they decrease first and recover once the strength of the body force progressively increases. In the relaminarization case Bf100Re45, the Reynolds shear stress profile $\sqrt{\overline{u_x'u_y'}}/u_b$ shows a magnitude close to zero, whereas fluctuations are still visible in the other three quantities. Surprisingly, the streamwise component $\sqrt{\overline{u_x'u_x'}}/u_b$ remains at a significant

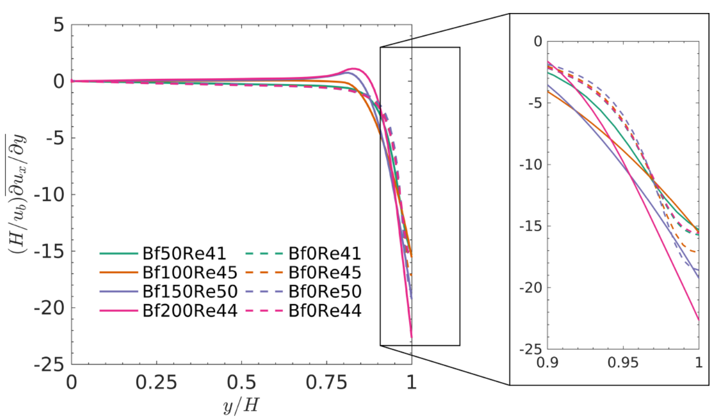

FIG. 6. Distribution of wall-normal streamwise-velocity gradient across the channel. The inset to the right shows the magnified view close to the wall.

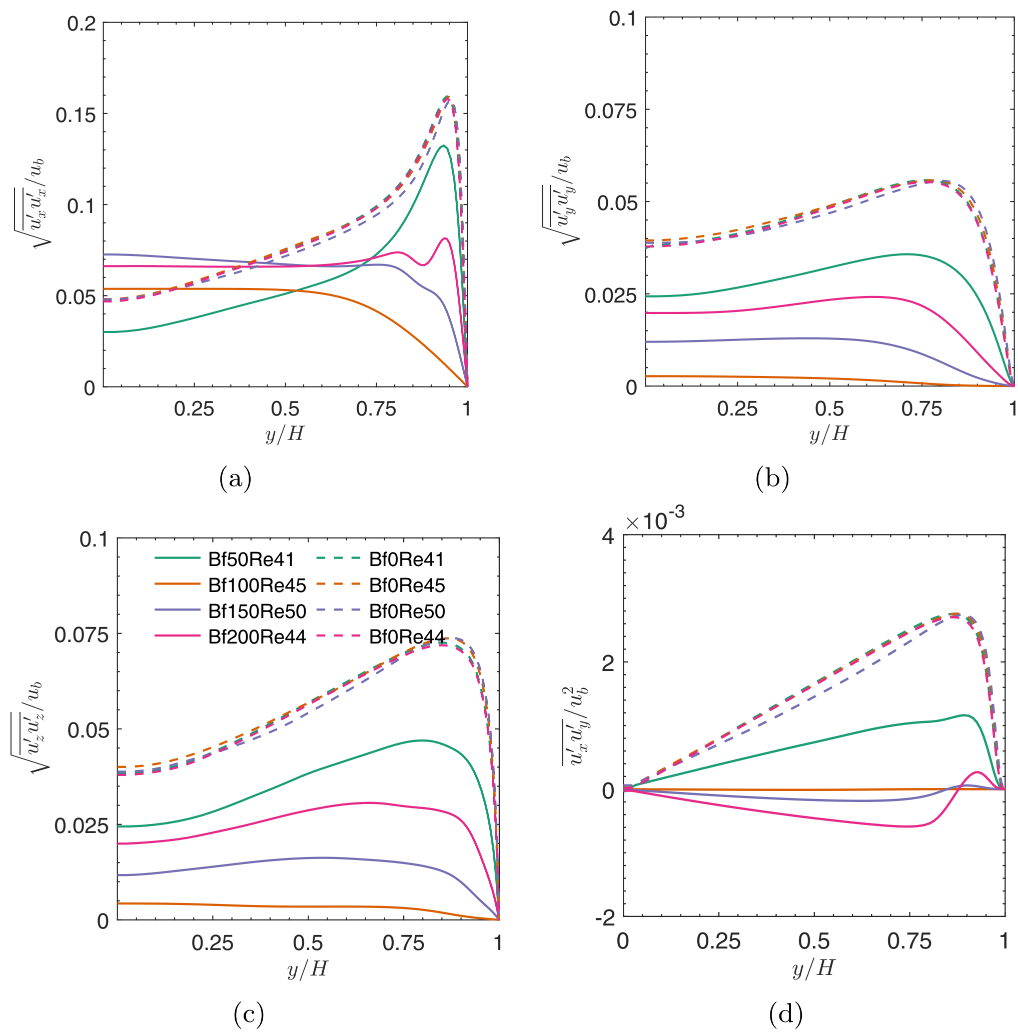

FIG. 7. Distribution of velocity fluctuations: (a) streamwise velocity, (b) wall-normal velocity, (c) spanwise velocity, and (d) turbulent shear stress across the channel.

fluctuation level in the bulk at approximately $y/H \leqslant 0.75$. The persistent streamwise fluctuations indicate a quasilaminar state in this case. In the recovered quasiturbulent state of case Bf200Re44, the streamwise fluctuation has two local maxima with a magnitude lower than that of the one maximum of the corresponding body-force-free reference case. These two peaks can be seen only in the streamwise velocity fluctuations and are not present in the wall-normal and spanwise profiles during the recovery. The dual peaks are produced by the nonmonotonic velocity profile in Fig. 5 and the corresponding shear profile in Fig. 6.

The turbulent shear stress in Fig. 7(d) shows an unusual trend with an increase of the body force. The small-amplitude body force case Bf50Re41 has a much lower turbulent shear stress than its reference case, which indicates a laminarescence—a precursor to relaminarization [15]. The shear stress decreases continuously and reaches almost zero for case Bf100Re45, where a fully developed laminar flow is observed. A further increase in the body force results in a positive peak near the wall and a negative peak in the bulk. Although the magnitude of both peaks is comparable, the negative turbulent shear covers the majority of the channel width.

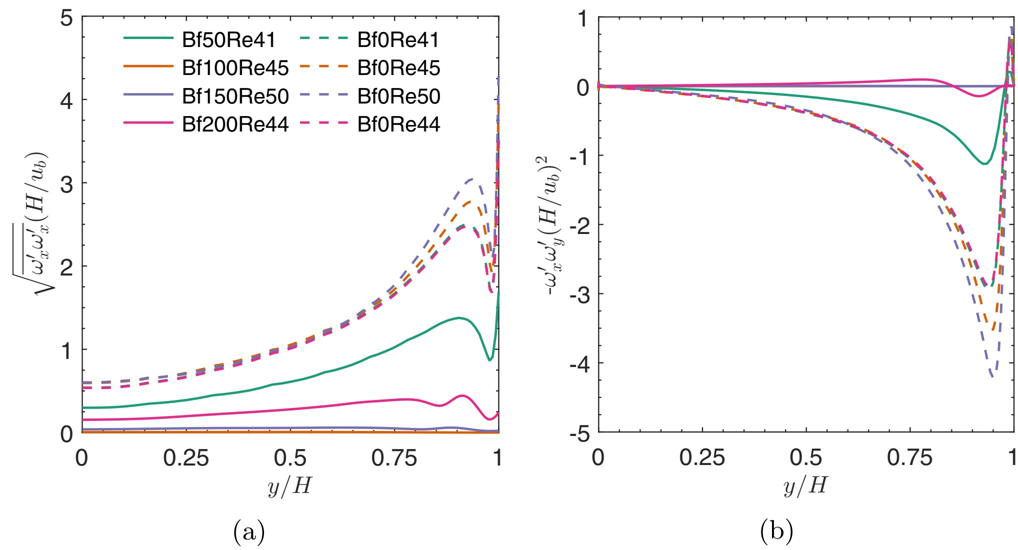

FIG. 8. Distribution of (a) streamwise vorticity fluctuations and (b) covariance of streamwise and spanwise vorticity across the channel.

Figure 8(a) depicts the rms streamwise vorticity ω_x fluctuations. The local minimum is close to the wall, and the global maximum is at the wall in all reference cases, which is consistent with the results of Kim *et al.* [26]. The local maximum is associated with the average location of the center of the streamwise vortices, and the local minimum indicates the presence of quasistreamwise vortices in the near-wall region [26–28]. The small-amplitude body force case reproduces the profiles of the force-free cases but with a reduced overall magnitude, indicating suppression of the streamwise vortices. The relaminarized case displays almost no fluctuations, as anticipated. The recovered flow case Bf200Re44 shows a different behavior, particularly near the wall. There is no maximum at the wall; instead, the mean profile has a local minimum at the usual location and then a maximum. The covariance of streamwise and wall-normal vorticity fluctuations is shown in Fig. 8(b). The recovered case Bf200Re44 yields a behavior similar to the corresponding Reynolds shear stress with an inflection point in the profile.

The near-wall turbulent structures are investigated by means of instantaneous flow visualizations for the body-force-influenced cases. Kim [29] has shown that streamwise vortices are formed and maintained by a self-sustaining process (also see [30]). These vortices interact with the mean shear and form streaks containing a spanwise modulation of the streamwise velocity. This process is known as the lift up. The streaks decay by linear instabilities, and streamwise vortices are newly generated from the streamwise decay products in a nonlinear process. This closed, cyclic, self-sustaining process does not require an explicit interaction with the outer part of the boundary layer. The cases simulated in the present study show an obvious effect of the steep-body force on the near-wall turbulence. Figure 9 illustrates the near-wall streamwise vortices for all cases. Apparently, the near-wall streamwise vortices are significantly weakened for cases with a body force (shown in red) compared to the reference cases at the same bulk Reynolds number. In Fig. 9(a), the weakly laminarized case shows vorticity isosurfaces similar to those of the reference case: most of them are concentrated near the wall, whereas the bulk region is free of vorticity. In Figs. 9(b) and 9(c), the vorticity in red is barely observable in the case of the quasilaminar and partially recovered state. If the turbulence is further increased as in Fig. 9(d), the streamwise vorticity appears at the position distant from the wall ($y/H \approx 0.7$), which is in contrast to the reference canonical channel flow. This phenomenon corresponds to the disappeared maximum of the vorticity fluctuation in

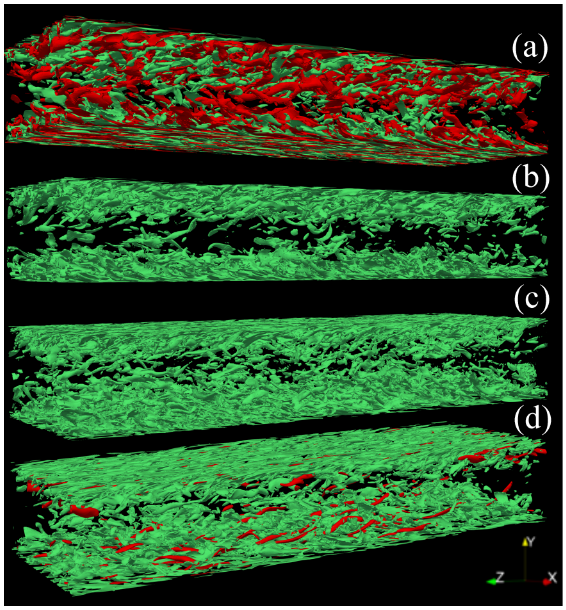

FIG. 9. Isosurface of streamwise vorticity: (a) cases Bf50Re41 and Bf0Re41, (b) cases Bf100Re45 and Bf0Re45, (c) cases Bf150Re50 and Bf0Re50, and (d) cases Bf200Re44 and Bf0Re44. Green isosurfaces stand for the reference case without additional body force, and red ones stand for the corresponding case with additional body force. For better visualization, the thresholds of the isosurface of the reference cases are taken at 2 times the ones for the corresponding body force case.

Fig. 8(a). Another distinction can be seen in terms of anisotropy. The vorticity structures in red appear tubelike, while the structures for the reference case in green are mostly disklike in Fig. 9(d). It indicates that the one-dimensional features of the turbulence start to dominate with the increase in body force. Additionally, the red and green structures of the body force and corresponding reference cases are tilted in opposite directions.

Figure 10 demonstrates the contours of the instantaneous fluctuations of the streamwise velocity in planes at $y/H = 0.89$ normalized by the bulk velocity. Both low- and high-speed streaks can be visualized for a small-amplitude body force case in Fig. 10(a). These streaks are not only elongated

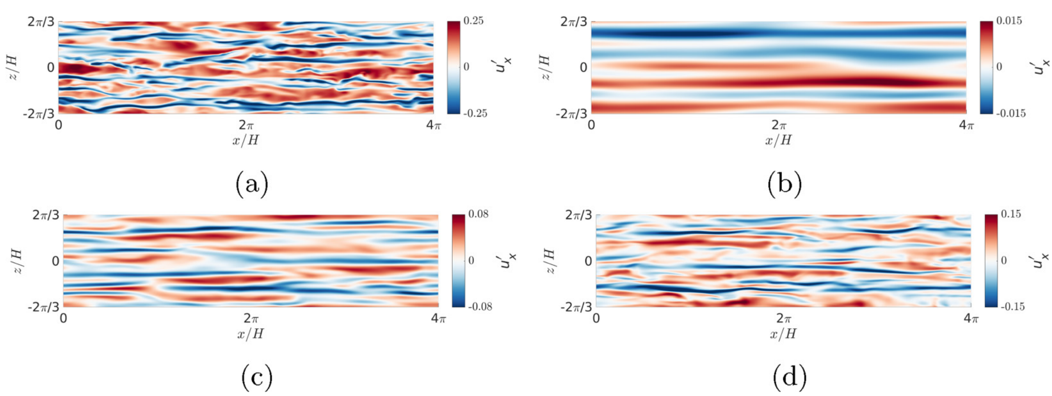

FIG. 10. Instantaneous streamwise velocity fluctuations in planes at $y/H = 0.89$ normalized by bulk velocity. (a) Case Bf50Re41. (b) Case Bf100Re45. (c) Case Bf150Re50. (d) Case Bf200Re44.

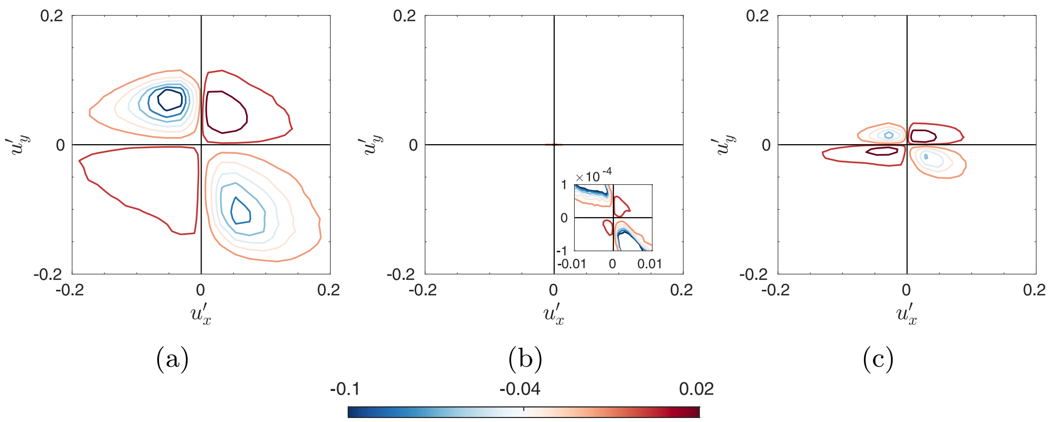

FIG. 11. Contours of weighted joint probability density functions of the fluctuating streamwise and wall-normal velocity component correlations at $y/H = 0.89$ wall. (a) Case Bf50Re41. (b) Case Bf100Re45. (c) Case Bf200Re44. The top right and bottom left panels in the inset magnify the contours.

but also damped in their magnitude; see case Bf100Re45 in Fig. 10(b). With larger body force as in case Bf200Re44, the streak breakdown is resumed, and the strength is also increased, as illustrated in Fig. 10(d). Thus, the cycle recommences with the larger body force, which is evident by the reappearance of streamwise vortices in Fig. 9(d). This explains the recovery, but in order to explain the observed inflection point, a quadrant analysis has to be performed, which we will present in the following.

B. Quadrant analysis

The quadrant analysis of the joint probability density functions (JPDFs) of the streamwise and wall-normal velocity fluctuations is discussed in this section. This statistical technique decomposes the Reynolds shear stress into quadrants, and each quadrant represents a specific event based on the sign of the streamwise and wall-normal velocity fluctuations [31]. Quadrant 1 is for $u'_x > 0$ and $u'_y > 0$; quadrant 2 is for $u'_x < 0$ and $u'_y > 0$ and so on. The events which take place in quadrant 2 (Q_2) and quadrant 4 (Q_4) are known as ejections and sweeps, respectively. Events corresponding to quadrant 1 (Q_1) and quadrant 3 (Q_3) represent the outward and inward interactions, respectively. Typically, Q_4 plays an important role close to the wall, and Q_2 events are the dominant contribution to the Reynolds shear stress farther away from the wall [32]. Figure 11 displays contours of $u'_x u'_y P(u'_x, u'_y)$ at a near-wall location of $y/H = 0.89$, where the maximal fluctuation energy of the reference cases is observed [see Fig. 7(a)]. As expected, Q_2 and Q_4 still contribute significantly for the small-amplitude body force case Bf50Re41 [see Fig. 11(a)]. With an increase of the body force amplitude, the Reynolds shear stress shows a reduction until the flow laminarizes completely [see Fig. 7(d)]. The genesis of turbulent attenuation comes from a reduction in ejection and sweep events. This reduction is caused by the disappearance of the streamwise vortices. Figure 11(b) shows that Q_2 and Q_4 disappear completely for a certain magnitude of the body force which corresponds to the elongated streaks with minor fluctuations. Ejections and sweeps reappear in Fig. 11(c), but at a smaller magnitude as in Fig. 11(a).

The turbulence recovery occurs at a higher body force with an inflection point of the Reynolds shear stress in the wall-normal direction [see again Fig. 7(d)]. Figure 12 shows contours of JPDFs of Reynolds shear stress at positive and negative maxima corresponding to Fig. 7(d). The ejections and sweeps are present now close to the wall [see Fig. 12(a)], while, interestingly, inward and outward interactions become stronger farther away from the wall [see Fig. 12(b)]. The significant difference in magnitude (see color bars) suggests more intensive inward and outward interactions

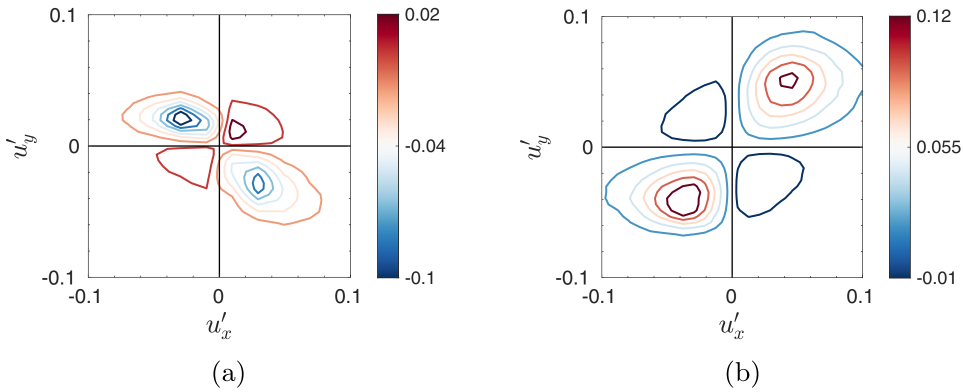

FIG. 12. Contours of weighted joint probability density functions of the Reynolds shear stress for case Bf200Re44 at (a) $y/H = 0.92$ and (b) $y/H = 0.74$.

in the bulk than near the wall. These qualitatively different JPDFs (Q_2 and Q_4 versus Q_1 and Q_3) in a single simulation case can be explained by the M-shaped velocity profile which we plotted in Fig. 5(a): the reverse velocity gradient in the bulk region enables high-speed velocity flow from the maximum mean velocity position to the channel center at $y/H = 1$ (inward direction), and in turn the lower-speed velocity in the channel center has to be compensated from the channel center to the maximum point (outward direction). On the other hand, the velocity gradient close to the wall is the same as in zero-body-force cases, which brings the high-speed velocity from the maximum mean velocity position towards the wall (sweep event), and a low-speed velocity fluid is ejected from the wall to the bulk (ejection event).

For the recovered case, $\omega'_x\omega'_y P(\omega'_x, \omega'_y)$ is shown in Fig. 13. Typically, Q_1 and Q_3 dominate the vorticity covariance. However, contributions from Q_2 and Q_4 become significant in the recovered flow case. It can also be seen that contours of streamwise vorticity fluctuations become broader than the contours of wall-normal vorticity fluctuations as one moves away from the wall.

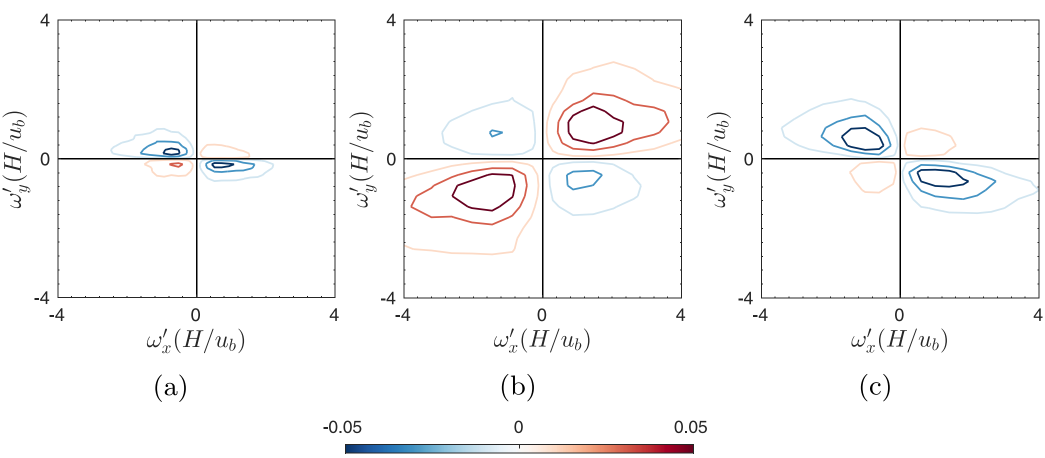

FIG. 13. Contours of weighted joint probability density functions of the fluctuating streamwise and wall-normal vorticity component for case Bf200Re44 at (a) $y/H = 0.98$, (b) $y/H = 0.91$, and (c) $y/H = 0.81$.

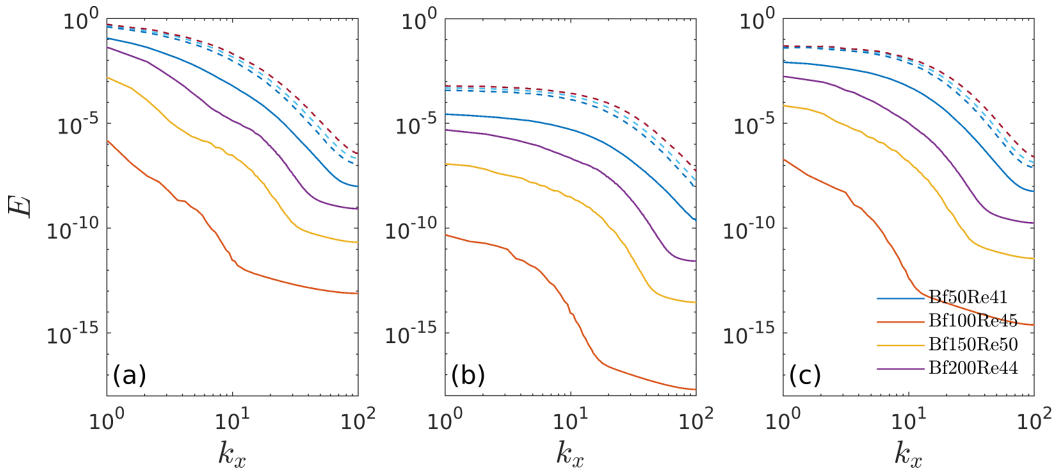

FIG. 14. One-dimensional spectra of (a) E_{uu}, (b) E_{vv}, and (c) E_{ww} at $y/H = 0.99$. Dashed lines show the corresponding reference cases which are found very closely together.

C. Spectral analysis

The turbulence energy spectra along the streamwise direction are now analyzed to investigate the effects of body force in the spectral space. Figure 14 illustrates the one-dimensional spectra for all three velocity components at $y/H = 0.99$ near the center plane for all simulation cases. The reference cases display an expected behavior with fluctuating energies E in all three velocity components, which decrease monotonically with an increase of the streamwise wave number k_x. An increase of the body force results in a reduction of the spectral energy across the whole wave number range. The recovery of turbulence is in line with a retrieval in energy. Interestingly, the energy-containing range vanishes in the spectra of the streamwise velocity for the relaminarized case Bf100Re45 in Fig. 14(a). Also, the tail of the spectra at high wave numbers is extended to lower k_x.

The drastic reduction in the energy at low wave numbers associated with the relaminarization can be explained by the ratio of production to dissipation (of turbulent kinetic energy k), which are given in homogeneous turbulence by

$$P_k = -\overline{u_i' u_j'}\,\overline{\frac{\partial u_i}{\partial x_j}}, \quad \epsilon_k = -\nu \overline{\frac{\partial u_i}{\partial x_j}\frac{\partial u_i}{\partial x_j}}. \tag{5}$$

Their ratio is shown in Fig. 15. The low body force case (case Bf50Re41) shows a typical behavior observed at low Reynolds numbers with a peak in the buffer layer. This peak vanishes during the relaminarization due to negligible turbulence production. It leads to a reduced energy density along with a vanished energy-containing range observed in Fig. 14. When the recovery starts in case Bf150Re50, two peaks appear in the ratio (see Fig. 15). A strong peak is located between the center and the wall of the channel, while a smaller second peak is located close to the wall. The strong peak is the result of the interaction events of the Reynolds shear stress. These events shift towards the wall for case Bf200Re44, which results in the second peak being much closer to the wall. In this case, another peak with the same strength also appears at the usual location (buffer layer), which is an outcome of sweep and ejection events which take place in this region.

Figure 16 shows the one-dimensional time-averaged, premultiplied spectra for velocity fluctuations E_{uu}, E_{vv}, and E_{ww} (where $u \mathrel{\hat{=}} u_x'$, $v \mathrel{\hat{=}} u_y'$, and $w \mathrel{\hat{=}} u_z'$) as a function of the half-channel width and streamwise wave numbers. For these spectra, we have taken the x-z plane at each y and performed Fourier transform in the x direction, followed by an average with respect to time and z direction. Figures 16(a)–16(c) depict the energy spectra for the fluctuating stream-

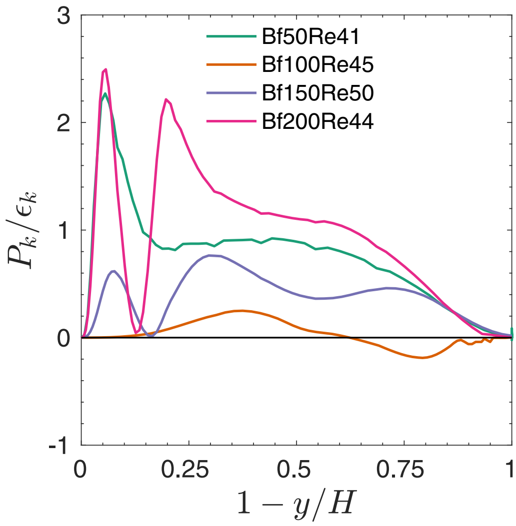

FIG. 15. Distribution of the ratio of production to dissipation of turbulent kinetic energy.

wise velocity field E_{uu} for three body-force-influenced flows. As stated by Hwang [33,34], the near-wall peak in streamwise velocity spectra suggests the presence of near-wall streaks. The peak in the wall-normal and spanwise spectra is in between the outer and near-wall regions, indicating the near-wall quasistreamwise vortices. The observations of the small-amplitude body force case [see Figs. 16(a), 16(d) 16(g)] are thus consistent with the findings of Hwang [33,34]. This peak in streamwise velocity spectra in Fig. 16(a) corresponds to the streaks in Fig. 10(a). The spectral maximum is shifted to the outer layer for larger body forces, which is visible in Fig. 16(b). Although low in magnitude, the peak is shifted away from the wall and observed in the bulk at $1 - y/H \approx 0.5$, which is visible in Fig. 16(b). The low wave number stands for an elongated streamwise extension. As the turbulence recovers [see Fig. 16(c)], the near-wall energetic motion is reconstructed with a blurred secondary peak distant from the wall.

The premultiplied spectra of the wall-normal and spanwise velocity components show a peak in between the outer and near-wall regions for the small-amplitude body force case, as shown in Figs. 16(d) and 16(g). Corresponding streamwise vortices are visible in Fig. 9(a). These peaks are also shifted during the relaminarization to the center of the channel. Figure 9(d) depicts the return of the vortices; consequently, spectra retrieve their original shapes [see Figs. 16(f) and 16(i)]. However, the double-peak behavior in the reconstructed streamwise spectra is not observed in the wall-normal and spanwise components.

Figure 17 shows the premultiplied Reynolds shear stress spectra. The region of maximal values is shrinking in case Bf100Re45, as shown in Fig. 17(b) along with a shift of the peak closer to the center. The two-peak behavior in the production-dissipation ratio P_k/ϵ_k, which we discuss in Fig. 15, can also be observed here in case Bf200Re44 as an extended region of peaks [see Fig. 17(c)]. The maximum closer to the wall is weaker than the maximum closer to the center. This stems from the Reynolds shear stress and is just opposite to that of Fig. 16(c).

D. Local flow topology

The quasilaminar and recovered states stemming from the body force should also manifest in the local flow topology. Therefore, the joint probability density function of the invariants of the velocity gradient tensor is analyzed in this section by employing the methodology developed by

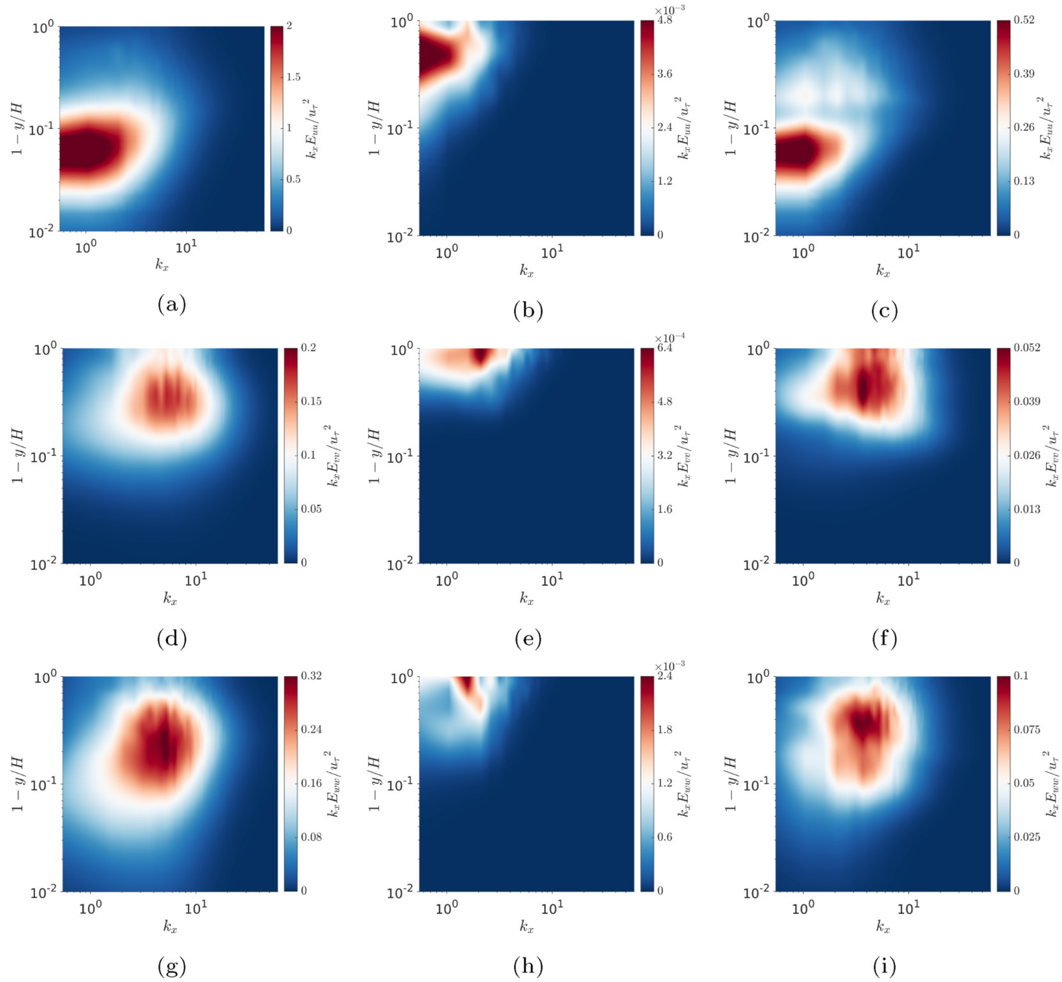

FIG. 16. Contours of premultiplied energy spectra of $E_{uu}(k_x, 1 - y/H)$, $E_{vv}(k_x, 1 - y/H)$, and $E_{ww}(k_x, 1 - y/H)$. The rows correspond to the three different components (a)–(c) for E_{uu}, (d)–(f) for E_{vv}, and (g)–(i) for E_{ww}. The columns correspond to three different cases: (a), (d), and (g) Bf50Re41, (b), (e), and (h) Bf100Re45, and (c), (f), and (i) Bf200Re44. Note also the different magnitudes in the corresponding color bars.

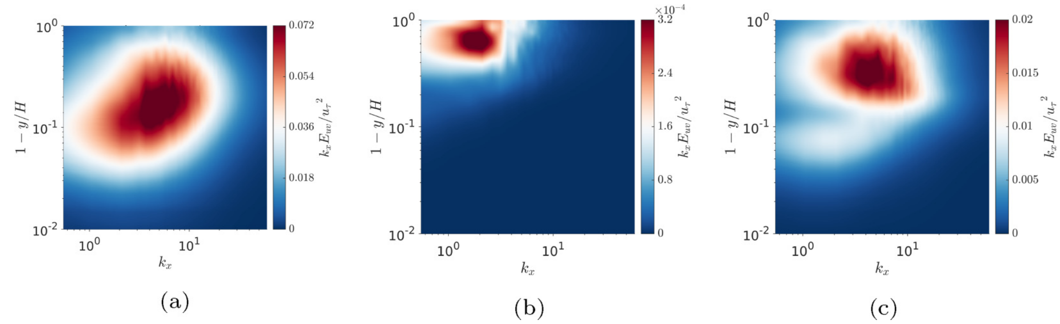

FIG. 17. Contours of premultiplied energy spectra of E_{uv}. Note the different magnitudes in the color bar. (a) Bf50Re41, (b) Bf100Re45, and (c) Bf200Re44.

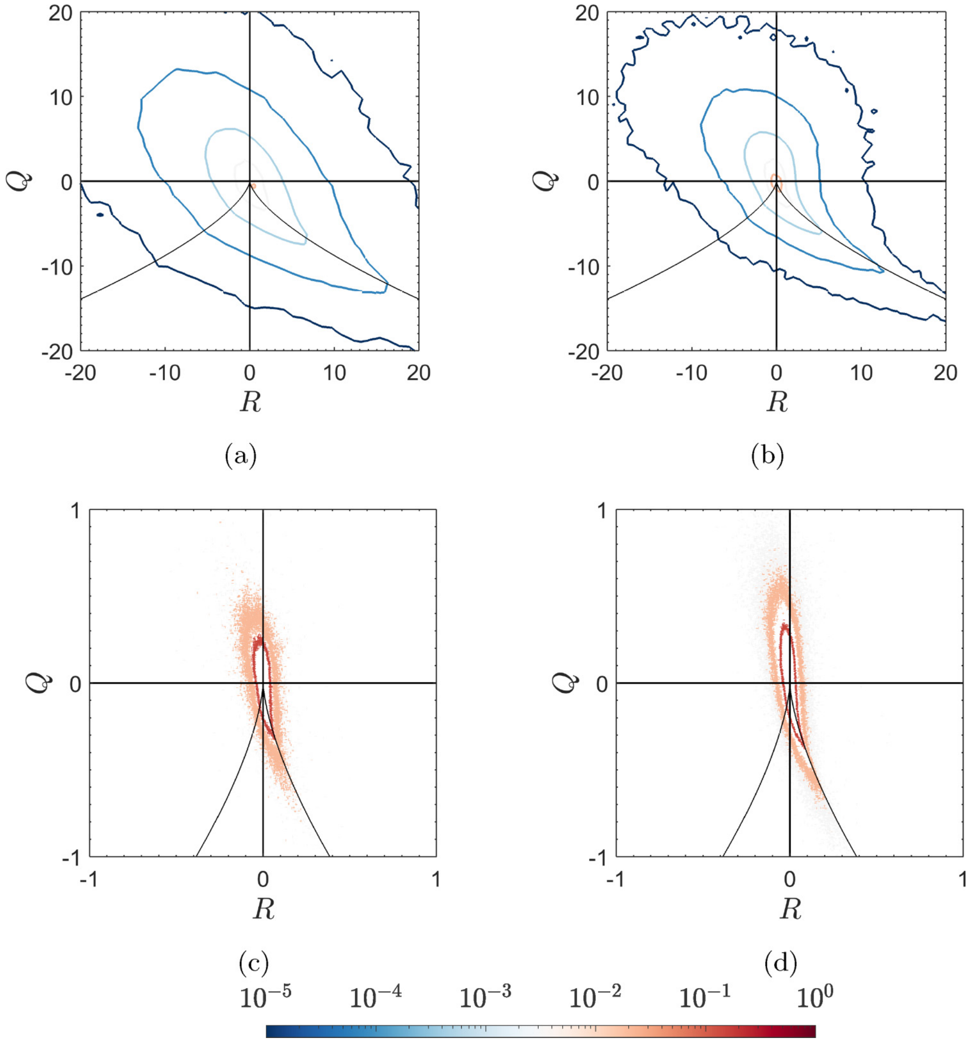

FIG. 18. Isocontours in logarithmic spacing of the JPDF of the second and third invariants of the velocity gradient tensor. (a) Case Bf0Re44, buffer layer ($5 \leqslant y^+ \leqslant 35$), (b) case Bf0Re44, log layer ($35 \leqslant y^+ \leqslant 150$), (c) case Bf200Re44, buffer layer ($5 \leqslant y^+ \leqslant 35$), and (d) case Bf200Re44, log layer ($35 \leqslant y^+ \leqslant 150$). The inclined black line represents the curve at which the discriminant is zero.

Chong *et al.* [35]. To be more specific, the second and third invariants, Q and R, will be combined in a JPDF. If velocity gradient tensor is given by $\mathbf{A} = \nabla \mathbf{u}$, then all three invariants are given by Eqs. (6)–(8). Therefore, the velocity gradient tensor is decomposed into the symmetric rate of the strain tensor $[S_{ij} = \frac{1}{2}(A_{ij} + A_{ji})]$ and the antisymmetric rotation tensor $[W_{ij} = \frac{1}{2}(A_{ij} - A_{ji})]$. Since the flow is incompressible, the first invariant P of the velocity gradient tensor A is exactly zero. All together,

$$P = -\mathrm{tr}(\mathbf{A}) = -S_{ii} = 0, \tag{6}$$

$$Q = \tfrac{1}{2}\{[\mathrm{tr}(\mathbf{A})]^2 - \mathrm{tr}(\mathbf{A}^2)\} = \tfrac{1}{2}[P^2 - S_{ij}S_{ji} - W_{ii}W_{ii}], \tag{7}$$

$$R = -\det(\mathbf{A}) = \tfrac{1}{3}[-P^3 - S_{ij}S_{jk}S_{ki} - 3W_{ij}W_{jk}S_{ki}]. \tag{8}$$

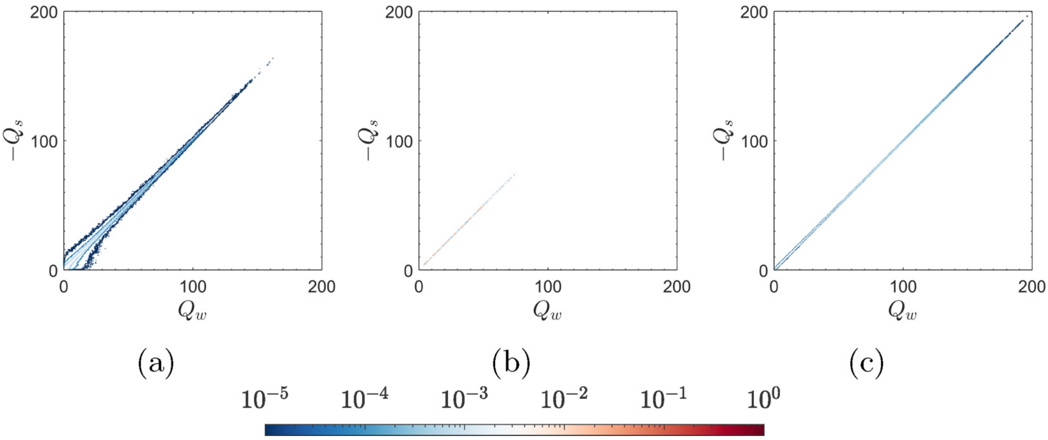

FIG. 19. Isocontours logarithmic of the PDF of the second invariant of the strain rate and rotation rate tensor in the buffer layer. (a) Case Bf50Re41. (b) Case Bf150Re50. (c) Case Bf200Re44.

The magnitudes of Q and R for the mean velocity profile are zero everywhere in the domain because any contribution is thus solely due to the turbulent velocity fluctuations [36]. Therefore, the relaminarized cases Bf100Re45 and Bf150Re50 have zero invariants and are omitted in the following discussion.

Figure 18 depicts the JPDF of Q and R for the recovered flow case Bf200Re44 and the corresponding reference case Bf0Re44 in the buffer layer ($5 \leqslant y^+ \leqslant 35$) and the logarithmic layer ($35 \leqslant y^+ \leqslant 150$). The flow without body force shows a teardrop shape outside the viscous sublayer with a statistical preference for the second and fourth quadrants, as seen in Fig. 18(a). This teardrop shape indicates that the flow has the most probable flow topology in the upper left quadrants, which corresponds to stable tubelike focus and stretching topology. For the recovered case, one can observe that the flow topology still shows a typical teardrop shape, even after the recovery when interaction events dominate, in both buffer and logarithmic layers. However, the magnitude is decreased significantly, compared to the reference case, which is due to the smaller number of fluctuations. Contrary to the reference case, the magnitude of Q and R increases in the logarithmic region. This results reaffirms our earlier observation of more fluctuations away from the wall. Moreover, the magnitude of Q is relatively high compared to R in the recovered flow case, indicating that the magnitude of strain is larger than the enstrophy in the flow.

Figure 19 illustrates the contours of the JPDF of the second invariant of the rate of strain tensor, $Q_s = \{[\mathrm{tr}(\mathbf{S})]^2 - \mathrm{tr}(\mathbf{S}^2)\}/2$, and the rotation tensor, $Q_w = \{[\mathrm{tr}(\mathbf{W})]^2 - \mathrm{tr}(\mathbf{W}^2)\}/2$, for all four cases with body force. The plot always follows a straight line at angle of 45° for a mean flow without any fluctuations. Data points on this line represent high dissipation complimented by high-enstrophy events [37]. Again, the small-amplitude body force case is qualitatively similar to its reference case. The JPDF is slightly skewed towards the axis with high enstrophy, and it indicates that solid-body rotation regions in the flow survive for a longer time than the unstable straining motion [38,39] [see Fig. 19(a)]. As soon as flow is relaminarized, all data points collapse on the straight line [Fig. 19(b)]. This is in line with a significantly reduced magnitude, which suggests that the flow lacks high-enstrophy and -dissipation events. Enstrophy and dissipation grow in the recovered flow cases [Fig. 19(c)].

To summarize this section, the body force changes the flow topology, especially when the flow is laminarized, which itself stems from the suppression of the self-sustaining turbulent cycle. However, the recovered turbulence is found to be in line with the characteristic flow topology. Note that the orientation of quadrants does not change, unlike in the earlier observation of Reynolds shear stress [refer back to Fig. 11(c)].

IV. CONCLUSIONS

In this work, a study of body-force-influenced flow in a channel has been performed by means of direct numerical simulations. We specifically focused on the piecewise linear body force profile which is common in flows of supercritical fluids. Here we decoupled the effects of variable thermophysical properties such that we can examine the sole contribution of an additional simple body force on the shear flow turbulence. The DNS was performed with a spectral/hp element method. A wall-normal varying body force was added to the streamwise momentum equation to suppress or reestablish the flow turbulence. The body force influences the Reynolds numbers; therefore, additional reference simulations were performed at the same Reynolds number without body force. Those cases were termed reference cases. The body force profile was motivated by a typical buoyancy force in supercritical fluids and was chosen at four different amplitudes, which allowed us to observe all three possible states in such channel flows. These are the laminarescent, relaminarized, and recovered shear flow.

The additional body force influences the mean velocity profile, thereby affecting the gradient of the mean velocity, which ultimately modulates the production of turbulence due to mean shear. Turbulent fluctuations decreased with an increase in the body force until the flow relaminarizes completely. For even higher body force amplitudes, the flow attempts to recover, and the Reynolds shear stress shows a peak for positive and negative values with an inflection point. This inflection point is a result of the dominance of the inward and outward events away from the wall, while the dominance of sweep and ejection events is close to the wall. In the relaminarized case, all events in a quadrant analysis disappear, which indicates negligible turbulent fluctuations about the mean flow. This leads also to the disappearance of streamwise vortical structures; the flow is dominated by elongated streamwise streaks. Two peaks in the ratio of production to dissipation of turbulent kinetic energy were observed during the recovery regime as a result of interaction events.

The streamwise spectra of the streamwise velocity fluctuations depict a drastic reduction in energy and a stretched tail in the dissipation range along with a vanishing energy-containing range. This occurred due to a negligible production which itself was the result of flow relaminarization. The premultiplied spectra of the velocity fluctuations were also analyzed in detail. The peak in the energy is shifted towards the outer layer, which indicates the disappearance of streaky structures from the flow in the near-wall region. Two peaks were also seen in the premultiplied spectra of streamwise velocity fluctuations and Reynolds shear stress in the flow recovery regime. Due to the body force, the flow topology shows a significant change compared to the force-free reference cases. Enstrophy and dissipation density become negligible in the relaminarized flow. Nonetheless, the typical teardrop shape reappears for the recovered flow.

Our work illustrated the role of body forces in influencing the shear flow turbulence while focusing on only supercritical fluids. Future work should focus on a unified framework for all kinds of forces which can augment the development of physics-informed reduced-order models such as Reynolds averaged Navier-Stokes and/or large-eddy simulations. Additionally, we demonstrated that body force can laminarize a fully developed turbulent shear flow. Thus, future flow control strategies might consider such piecewise linear profiles.

ACKNOWLEDGMENTS

The first author appreciates the support from the Deutsche Forschungsgemeinschaft (DFG) through Grant No. SCHU 1410/30-1. X.C. and B.W. extend their gratitude to the Ministerium für Wissenschaft, Forschung und Kunst of Baden-Württemberg (Germany) for the financial support within the project DISS (Data-Integrated Simulation Science). All authors gratefully appreciate the access to the high-performance computing facility Hazel Hen in HLRS, Stuttgart, under projects DNSTHTSC and PoroDNS.

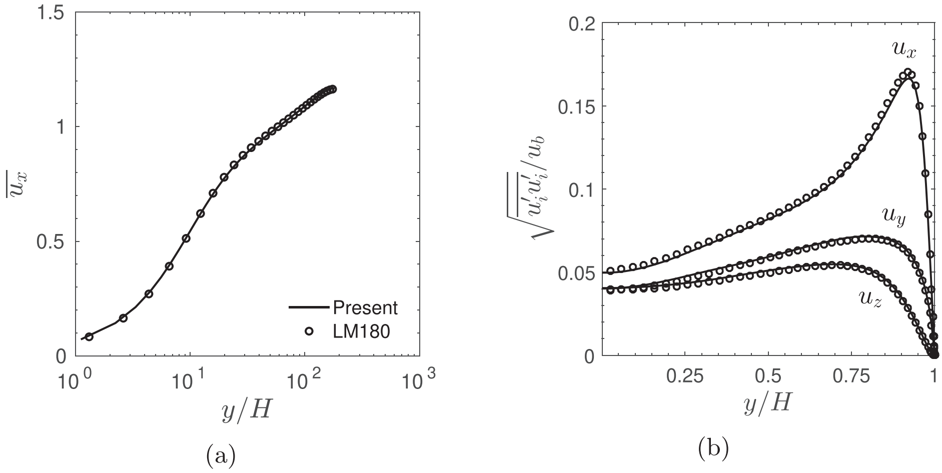

FIG. 20. Verification of the present DNS code with Lee and Moser [40]: (a) mean streamwise velocity profile and (b) rms fluctuations of velocity.

APPENDIX: CODE VERIFICATION

The incompressible channel flow at a friction Reynolds number of 182 and a bulk Reynolds number of 2857 is verified with the well-known incompressible channel flow DNS data of Lee and Moser [40] (labeled LM180). The corresponding simulations were performed with the NEKTAR++ code. Figure 20 shows the wall-normal profiles for the mean velocity and the rms velocity fluctuations normalized with the bulk velocity u_b. Very good agreement can be observed in Fig. 20 for the incompressible flow case.

The present study takes advantage of the spectral analysis. Therefore, a verification study was also performed for the spectra, as shown in Fig. 21 for $y^+ = 30$. The comparison is made between the classical DNS data of Moser *et al.* [41] (labeled MKM) and more recent data obtained by Vreman and Kuerten [42]. Good agreement can be seen for all three spectra.

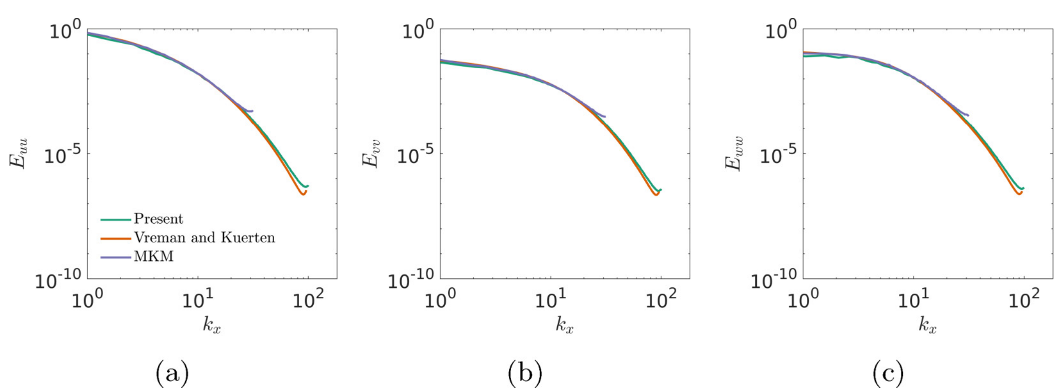

FIG. 21. Verification of the present DNS code with results from Moser *et al.* [41] and Vreman and Kuerten [42]: (a) E_{uu}, (b) E_{vv}, and (c) E_{ww} at $y^+ = 30$.

[1] J. W. R. Peeters, R. Pecnik, M. Rohde, T. H. J. J. van der Hagen, and B. J. Boersma, Characteristics of turbulent heat transfer in an annulus at supercritical pressure, Phys. Rev. Fluids **2**, 024602 (2017).

[2] S. Pandey, X. Chu, and E. Laurien, Investigation of in-tube cooling of carbon dioxide at supercritical pressure by means of direct numerical simulation, Int. J. Heat Mass Transfer **114**, 944 (2017).

[3] A. Patel, B. J. Boersma, and R. Pecnik, Scalar statistics in variable property turbulent channel flows, Phys. Rev. Fluids **2**, 084604 (2017).

[4] J. H. Bae, J. Y. Yoo, and H. Choi, Direct numerical simulation of turbulent supercritical flows with heat transfer, Phys. Fluids **17**, 105104 (2005).

[5] X. Chu and E. Laurien, Flow stratification of supercritical CO_2 in a heated horizontal pipe, J. Supercrit. Fluids **116**, 172 (2016).

[6] J. D. Jackson, M. A. Cotton, and B. P. Axcell, Studies of mixed convection in vertical tubes, Int. J. Heat Fluid Flow **10**, 2 (1989).

[7] S. Pandey, X. Chu, E. Laurien, and B. Weigand, Buoyancy induced turbulence modulation in pipe flow at supercritical pressure under cooling conditions, Phys. Fluids **30**, 065105 (2018).

[8] A. Steiner, On the reverse transition of a turbulent flow under the action of buoyancy forces, J. Fluid Mech. **47**, 503 (1971).

[9] H. Nemati, A. Patel, B. J. Boersma, and R. Pecnik, Mean statistics of a heated turbulent pipe flow at supercritical pressure, Int. J. Heat Mass Transfer **83**, 741 (2015).

[10] X. Chu, E. Laurien, and D.M. McEligot, Direct numerical simulation of strongly heated air flow in a vertical pipe, Int. J. Heat Mass Transfer **101**, 1163 (2016).

[11] T. Wetzel and C. Wagner, Buoyancy-induced effects on large-scale motions in differentially heated vertical channel flows studied in direct numerical simulations, Int. J. Heat Fluid Flow **75**, 14 (2019).

[12] E. Rinaldi, A. Patel, P. Schlatter, and R. Pecnik, Linear stability of buffer layer streaks in turbulent channels with variable density and viscosity, Phys. Rev. Fluids **2**, 113903 (2017).

[13] A. Patel, J. W. R. Peeters, B. J. Boersma, and R. Pecnik, Semi-local scaling and turbulence modulation in variable property turbulent channel flows, Phys. Fluids **27**, 095101 (2015).

[14] S. He, K. He, and M. Seddighi, Laminarisation of flow at low Reynolds number due to streamwise body force, J. Fluid Mech. **809**, 31 (2016).

[15] K. R. Sreenivasan, Laminarescent, relaminarizing and retransitional flows, Acta Mech. **44**, 1 (1982).

[16] T. W. Berger, J. Kim, C. Lee, and J. Lim, Turbulent boundary layer control utilizing the Lorentz force, Phys. Fluids **12**, 631 (2000).

[17] B. E. Launder, Laminarization of the turbulent boundary layer in a severe acceleration, J. Appl. Mech. **31**, 707 (1964).

[18] R. Narasimha and K. R. Sreenivasan, Relaminarization in highly accelerated turbulent boundary layers, J. Fluid Mech. **61**, 417 (1973).

[19] C. D. Cantwell, D. Moxey, A. Comerford, A. Bolis, G. Rocco, G. Mengaldo, D. De Grazia, S. Yakovlev, J.-E. Lombard, D. Ekelschot, B. Jordi, H. Xu, Y. Mohamied, C. Eskilsson, B. Nelson, P. Vos, C. Biotto, R. M. Kirby, and S. J. Sherwin, Nektar++: An open-source spectral/hp element framework, Comput. Phys. Commun. **192**, 205 (2015).

[20] C. D. Cantwell, S. J. Sherwin, R. M. Kirby, and P. H. J. Kelly, From h to p efficiently: Strategy selection for operator evaluation on hexahedral and tetrahedral elements, Comput. Fluids **43**, 23 (2011).

[21] G. E. Karniadakis, M. Israeli, and S. A. Orszag, High-order splitting methods for the incompressible Navier-Stokes equations, J. Comput. Phys. **97**, 414 (1991).

[22] N. Yadav, S. W. Gepner, and J. Szumbarski, Flow dynamics in longitudinally grooved duct, Phys. Fluids **30**, 104105 (2018).

[23] X. Chu, G. Yang, S. Pandey, and B. Weigand, Direct numerical simulation of convective heat transfer in porous media, Int. J. Heat Mass Transfer **133**, 11 (2019).

[24] H. Xu, J.-E. W. Lombard, and S. J. Sherwin, Influence of localised smooth steps on the instability of a boundary layer, J. Fluid Mech. **817**, 138 (2017).

[25] H. Xu, S. M. Mughal, E. R. Gowree, C. J. Atkin, and S. J. Sherwin, Destabilisation and modification of Tollmien-Schlichting disturbances by a three-dimensional surface indentation, J. Fluid Mech. **819**, 592 (2017).

[26] J. Kim, P. Moin, and R. Moser, Turbulence statistics in fully developed channel flow at low Reynolds number, J. Fluid Mech. **177**, 133 (1987).

[27] P. Moin and J. Kim, Numerical investigation of turbulent channel flow, J. Fluid Mech. **118**, 341 (1982).

[28] C. H. Crawford and G. E. Karniadakis, Reynolds stress analysis of EMHD-controlled wall turbulence. Part I. Streamwise forcing, Phys. Fluids **9**, 788 (1997).

[29] J. Kim, Physics and control of wall turbulence for drag reduction, Philos. Trans. Math Phys. Eng. Sci. **369**, 1396 (2011).

[30] F. Waleffe, On a self-sustaining process in shear flows, Phys. Fluids **9**, 883 (1997).

[31] J. M. Wallace, Quadrant analysis in turbulence research: History and evolution, Annu. Rev. Fluid Mech. **48**, 131 (2016).

[32] J. M. Wallace and R. S. Brodkey, Reynolds stress and joint probability density distributions in the u-v plane of a turbulent channel flow, Phys. Fluids **20**, 351 (1977).

[33] Y. Hwang, Statistical structure of self-sustaining attached eddies in turbulent channel flow, J. Fluid Mech. **767**, 254 (2015).

[34] Y. Hwang, Near-wall turbulent fluctuations in the absence of wide outer motions, J. Fluid Mech. **723**, 264 (2013).

[35] M. S. Chong, A. E. Perry, and B. J. Cantwell, A general classification of three-dimensional flow fields, Phys. Fluids **2**, 765 (1990).

[36] H. M. Blackburn, N. N. Mansour, and B. J. Cantwell, Topology of fine-scale motions in turbulent channel flow, J. Fluid Mech. **310**, 269 (1996).

[37] J. Soria, R. Sondergaard, B. J. Cantwell, M. S. Chong, and A. E. Perry, A study of the fine-scale motions of incompressible time-developing mixing layers, Phys. Fluids **6**, 871 (1994).

[38] M. S. Dodd and L. Jofre, Small-scale flow topologies in decaying isotropic turbulence ladden with finite-size droplets, Phys. Rev. Fluids **4**, 064303 (2019).

[39] A. Ooi, J. Martin, J. Soria, and M. S. Chong, A study of the evolution and characteristics of the invariants of the velocity-gradient tensor in isotropic turbulence, J. Fluid Mech. **381**, 141 (1999).

[40] M. Lee and R. D. Moser, Direct numerical simulation of turbulent channel flow up to $Re_\tau \approx 5200$, J. Fluid Mech. **774**, 395 (2015).

[41] R. D. Moser, J. Kim, and N. N. Mansour, Direct numerical simulation of turbulent channel flow up to $Re_\tau = 590$, Phys. Fluids **11**, 943 (1999).

[42] A. W. Vreman and J. G. M. Kuerten, Comparison of direct numerical simulation databases of turbulent channel flow at $Re_\tau = 180$, Phys. Fluids **26**, 015102 (2014).